





RESEARCH ARTICLE | SEPTEMBER 04 2024

Diffusion mechanisms for spinel ferrite NiFe_2O_4 by using kinetic activation–relaxation technique

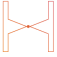
Oscar A. Restrepo   ; Charlotte S. Becquart  ; Normand Mousseau 





J. Chem. Phys. 161, 094307 (2024)


<https://doi.org/10.1063/5.0220397>




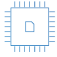
 Nanotechnology & Materials Science

 Optics & Photonics

 Impedance Analysis

 Scanning Probe Microscopy

 Sensors

 Failure Analysis & Semiconductors

Diffusion mechanisms for spinel ferrite NiFe_2O_4 by using kinetic activation–relaxation technique

Cite as: J. Chem. Phys. 161, 094307 (2024); doi: 10.1063/5.0220397

Submitted: 24 May 2024 • Accepted: 21 August 2024 •

Published Online: 4 September 2024



View Online



Export Citation



CrossMark

Oscar A. Restrepo,^{1,a)}  Charlotte S. Becquart,²  and Normand Mousseau³ 

AFFILIATIONS

¹Biophysics Group, Institute of Physics, University of Antioquia, 050010 Medellín, Colombia

²Univ. Lille, CNRS, INRAE, Centrale Lille, UMR 8207 - UMET - Unité Matériaux et Transformations, F-59000 Lille, France

³Département de physique, Regroupement québécois sur les matériaux de pointe, and Institut Courtois, Université de Montréal, Case Postale 6128, Succursale Centre-Ville, Montréal, Quebec H3C 3J7, Canada

^{a)} Author to whom correspondence should be addressed: ores77@gmail.com

ABSTRACT

Mass transport in bulk spinel ferrites NiFe_2O_4 is studied computationally using the kinetic activation–relaxation technique (k-ART), an off-lattice kinetic Monte Carlo algorithm. Diffusion mechanisms—difficult to observe with molecular dynamics—are described by k-ART. Point defects are assumed to be responsible for ionic diffusion; thus, both cation and anion defects are investigated. This work focuses on vacancies and interstitials by comparing their properties with two Buckingham potential parameterizations: one with nominal charges and the other with partial charges. Both potentials are corrected at short distances, thus allowing interstitial diffusion and avoiding the catastrophic infinite energies appearing with Buckingham at short distances. The energy landscape along different pathways is described in detail. Both potentials predict the same mechanisms but different migration energies. Mechanisms by which a normal spinel is transformed to an inverse spinel via cation diffusion are unveiled, and diffusion coefficients are predicted. We find that interstitial Ni diffusion involves the movement of two Ni ions and that O interstitials trigger a collective diffusion of O ions, while an O vacancy diffuses by an O ion moving to the center of a cuboctahedron.

Published under an exclusive license by AIP Publishing. <https://doi.org/10.1063/5.0220397>

I. INTRODUCTION

Spinel ferrites, such as NiFe_2O_4 (NFO) and ZnFe_2O_4 , are associated with several technological applications, such as a promising anode catalyst material in electrochemical water splitting used in the field of renewable energy sources.¹ In general, spinel materials are also considered for nuclear applications due to their resistance to radiation damage caused by neutrons and light ions.^{2,3} Spinel ferrites are used in steel fabrication, metal corrosion oxidation, spintronic devices, batteries, etc.^{4–9} They are of particular importance due to their low cost, high catalytic activity, durability, and more.^{10,11} In all these applications, understanding of the diffusion properties is of radical importance as ionic diffusion plays a major role in determining the rate process of solid-state reactions, so some interesting studies have been done in this way using density functional theory (DFT).^{10,12–14}

Because the spinel structure has more than one cation in its formula, these compounds have a complex potential energy

surface and their defects are difficult to characterize. Although simple migration routes in a normal spinel have been known for a long time,^{15,16} many diffusion mechanisms for typical point defects are still unknown. Because of the role of defect diffusion—vacancies or interstitials—for determining the properties of materials in numerous applications, there has been a considerable effort to quantify the relevant migration mechanisms via atomistic simulations. For instance, DFT studies of cation diffusion in Fe_3O_4 , CoFe_2O_4 , and NiFe_2O_4 spinel ferrites have shown simple diffusion mechanisms.¹² However, other diffusion mechanisms may exist and play a key role in the spinel formation as a normal or inverse structure, as spinel ferrites NFO can be synthesized by different experimental methods,^{8,17–21} but these have not yet been identified.

In general, a spinel is described by the formula AB_2O_4 .²² For a nickel-ferrite, in the normal spinel case, Ni^{2+} and Fe^{3+} fill A and B sites, respectively, but from the experimental viewpoint, the most chemically stable structure is the inverse spinel where the Fe^{3+} atoms

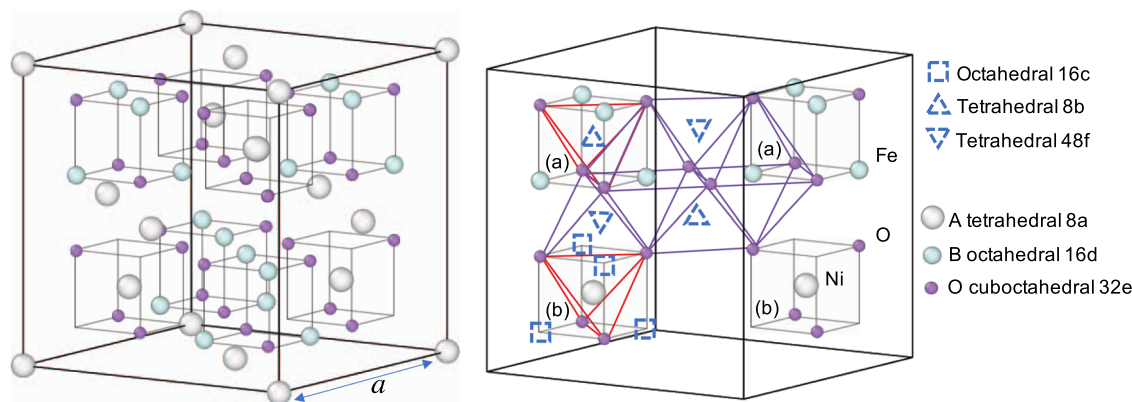


FIG. 1. On the left, a normal spinel cell of size a , small cubes are drawn as a guide. On the right, octahedral and tetrahedral figures formed inside the spinel cell (half of atoms inside plus atoms at all faces are removed for simplicity). Lattice positions are given by spheres; the interstitial equipoints are indicated by dashed squares [octahedral sites at corners of cube (b)] and triangles and inverted triangles (tetrahedral sites).

fill all 8 A-sites and Ni^{2+} and Fe^{3+} randomly fill the 16 B-sites. The conventional unit cell of an ideal spinel structure consists of eight different planes and has 56 atoms; the cell with the origin at the $43m$ point symmetry is shown in Fig. 1. Sickafus and Wills describe the spinel structure and the symmetric points where interstitials should be located in the unit cell.²² These equipoints (Wyckoff notation) include two tetrahedral 8b points, 12 tetrahedral 48f points, and four octahedral 16c points. Some of these sites are represented as dashed squares and triangles in Fig. 1. A simple observation of these equipoints suggests some obvious diffusion paths, e.g., interstitial ions jumping from octahedral site 16c to 16c via the tetrahedral site 48f, in agreement with the DFT.¹² Furthermore, the anion parameter u has an ideal value of $u_{43m} = 3/8$, but u is experimentally larger, with important consequences for self-diffusion in NFO according to Sickafus:²² for a perfect normal spinel (no defects), a B-site cation can make a jump to the nearest octahedral site 16c (multiplicity 6), moving directly to the octahedral point, or migrate via a nearest tetrahedral site 8b or 48f (multiplicity 8) (see Fig. 1). For an ideal cubic close packed (ccp) arrangement,²² the latter route should be preferred, as the former involves the movement of neighboring anions. However, for NFO, $u_{43m} > 0.385$, so competition between the two pathways should be expected. Similarly, for tetrahedral A-sites, diffusion to a nearest tetrahedral site 48f (multiplicity 6) should occur by a direct jump or by migration via a nearest octahedral site 16c (multiplicity 4); again, the latter route should be preferred. Similarly, when considering point defect diffusion, u plays a relevant role and, as we will see in Sec. III, diffusion mechanisms in a normal spinel NFO can be more complex; this is particularly true for O interstitials.

For simple systems, diffusion mechanisms and associated migration energies are usually investigated using classical molecular dynamics (MD).²³ While Arrhenius plots allow the identification of diffusion coefficients and barrier energies, MD does not ensure that all physically relevant diffusion mechanisms are considered, since these can occur on timescales longer than allowed by MD integration. To circumvent this limitation, several investigations have been carried out to study spinel migration using more

advanced tools such as kinetic Monte Carlo (KMC)²⁴ and temperature accelerated dynamics (TAD).²⁵ Both methods assume harmonic transition state theory, with barriers being calculated by double-ended methods such as with the climbing-image nudged elastic band (CI-NEB) method.²⁶ For instance, TAD calculates high temperature MD trajectories and uses them to extrapolate behavior to a lower temperature of interest and, once a transition from one state to any neighboring state is detected, the trajectory is interrupted and the barrier for that process is calculated using the CI-NEB method.²⁵ In this way, the long-time behavior of defects (interstitial transport properties) in spinel systems such as MgAl_2O_4 , MgGa_2O_4 , MgIn_2O_4 , and MgAlGaO_4 was analyzed.^{2,27} Another simple case is that of substitutional ions in doped spinel systems. For instance, in a first-principles study of Li-ion diffusion in the Fe-doped halospinel $\text{Li}_2\text{Sc}_{2/3}\text{Cl}_4$, a substitutional Li is located at 8a and 16d sites, and NEB shows that when Fe is located at 16d sites, the Li-ion diffuses through only 16d sites, as opposed to the 8a-to-8a pathway with a higher migration energy.²⁸

Here, we select to use the kinetic activation-relaxation technique (k-ART), an open-ended method and off-lattice kinetic Monte Carlo algorithm, to study the migration paths of spinel defects computationally. The k-ART is developed to explore the energy landscape and long-time kinetics of complex systems at the atomic scale, fully including long-range elastic events and disordered environments.^{29–32} As an open-ended method, at each step, k-ART starts from one local minimum and looks for all the adjacent saddles and minima, providing a rich exploration and a detailed description of diffusion paths.

Using k-ART, we characterize the energy landscape of vacancy and interstitial defects diffusing into a bulk spinel crystal. Following the evolution of the energy landscape over timescales ranging from tenths of microseconds to seconds or years, we generate a detailed picture of the various mechanisms. We start with Sec. II: we briefly describe the k-ART method followed by sample construction and implemented potentials. We then examine the dominant mechanisms and migration energies for vacancies and interstitials before offering conclusions.

II. METHODOLOGY

A. Overview of k-ART

In kinetic Monte Carlo (KMC), an event is defined as the transition from one state to another state in the configurational space by crossing a given barrier energy and is fully characterized by three atomic configurations: the initial minimum, the saddle point, and the final minimum. To simplify the storage ($3N$ atoms per event) and make event cataloging possible, k-ART uses a topological characterization of the local environment surrounding each atom to classify these configurations as explained below.

While k-ART has been discussed in many papers,^{29–32} we give a brief summary of the algorithm for convenience: (1) At each KMC step, the local topology of each atom is computed by creating a graph connecting a list of atoms within a distance of 2.7 Å of each other and enclosed in a sphere of 6 Å surrounding the selected atom. The graph is then analyzed using the NAUTY code,^{33,34} which returns a number classifying the topology around that atom. (2) If the topology is known, events associated with it are inserted in an active list; if the topology is new, event searches are launched using the activation–relaxation technique (ART nouveau), an open-ended method, to identify diffusion mechanisms and energy barriers.^{35–37} (3) A first classification of the active events is generated, with events ordered by their rate, $r_i = \nu e^{E_b/k_b T}$, where ν is a prefactor set to a constant 10^{13} s^{-1} , k_b is the Boltzmann constant, T is the temperature, and $E_b = E_{sad} - E_{min}$, is the activation energy, in which E_{min} and E_{sad} are the energies at an initial minimum and the saddle (i.e., the barrier crossed between two adjacent minima). (4) All events with an occurrence probability of 1 in 10 000 or higher are fully reconstructed and relaxed, using ART nouveau, to ensure that elastic and local deformation effects are exactly considered.³¹ (5) The time step is obtained from a Poisson distribution, $\Delta t = -\log(\mu)/\sum_i r_i$, where μ is a random number in (0,1), and an event is randomly selected with a weight proportional to its rate, according to standard KMC.²⁴ After an event is selected and applied, we repeat the cycle up to a predefined number of steps or maximum total time.

During simulations, flickering states may occur. These correspond to the states of similar energy separated by low energy barriers, which can dominate event-based KMC simulations and

slow system evolution to a halt; they are avoided by using the basin-auto-constructing mean rate method (bac-MRM), which computes an on-the-fly statistically correct analytic solution of the connected flickering states and their average escape rate as the energy landscape is explored.^{31,38} The square displacement is computed according to

$$\Delta r^2(t_n) = \sum_{i=1}^N (\mathbf{x}_i(t_n) - \mathbf{x}_i(0))^2, \quad (1)$$

where N is the number of particles and $\mathbf{x}_i(t_n)$ is the position of atom i at KMC step n and time t_n . The diffusion coefficient over a total of M steps is computed using Einstein's formula as follows:

$$D = \left(\frac{1}{6t_M^2} \right) \sum_{n=1}^M \Delta r^2(t_n) \Delta t_n, \quad (2)$$

where a time average is considered according to the ergodic hypothesis.

B. Sample construction

For the sake of simplicity, in this study, we have only considered the analysis of diffusion in a normal spinel configuration with a box of $2 \times 2 \times 2$ unit cells and 448 atoms, required to account for the effects produced by the stress associated with defects. For the calculation of the vacancy energies, boxes up to $8 \times 8 \times 8$ are used to ensure convergence.

C. Force-field

For the study of ionic systems, we have found several empirical potentials.^{39,40} We use k-ART coupled with Buckingham potentials to study diffusion defects in spinel systems. In the typical implementation of this type of potential, infinite energies appear at short distances. Note that normally this is not a problem, since the aim is often to describe a structure at a minimum energy or dynamics at a low energy, but in collisions, high temperature, or in our case for interstitial diffusion, it is a problem because the potential becomes attractive at smaller distances. Therefore, a modified short-range part of the potential is used to avoid unreasonable results,^{16,41} e.g., in interstitial diffusion where oxygen is particularly sensitive to

TABLE I. Buckingham parameters for NiFe₂O₄: Buck-1 partial charges and Buck-2 nominal charges. For FeFe, NiNi, and NiFe, only Coulomb terms are used.

NFO, Buck-1. ⁴² Ions adopt partial charges.									
Pair	z_i	z_j	A_{ij} (eV)	ρ_{ij} (Å)	C_{ij} (eV Å ⁶)	B_{ij} (eV Å ⁿ)	D_{ij} (eV/Å ²)	n	r_0 (Å)
O–O	–1.2	–1.2	2029.2204	0.343 645	192.58	46.462	–0.326 05	3.430	1.9376
NiO	1.2	–1.2	12 987.7832	0.203 164	35.994	73.158	–14.550	3.024	1.0274
FeO	1.8	–1.2	11 777.0703	0.207 132	21.642	104.203	–32.110	2.670	0.9302
NFO, Buck-2. ^{43,44} Ions adopt nominal charges. B_{ij} , D_{ij} , and n fitted here.									
O–O ⁴⁴	–2	–2	9547.96	0.2192	32	172.654 926 10	–107.322 474 82	0.605 523 19	0.8900
NiO ⁴³	2	–2	775.0	0.3250	0	98.450 187 610	–122.818 978 45	1.000 970 20	0.4600
FeO ⁴⁴	3	–2	1414.6	0.3128	0	169.192 731 98	–229.585 000 58	1.020 247 78	0.4500

this correction as infinite energies may appear. So, the potential is written as follows:

$$U_{ij}(r) = \begin{cases} \frac{z_i z_j e^2}{4\pi\epsilon_0 r_{ij}} + A_{ij} \exp\left(\frac{-r_{ij}}{\rho_{ij}}\right) - \frac{C_{ij}}{r_{ij}^6} & \text{if } r_{ij} \geq r_0, \\ \frac{z_i z_j e^2}{4\pi\epsilon_0 r_{ij}} + D_{ij} r_{ij}^2 + \frac{B_{ij}}{r_{ij}^n} & \text{if } r_{ij} < r_0, \end{cases} \quad (3)$$

where B_{ij} , D_{ij} , and n are parameters fitted for each ion. We test two parameterizations here: the first, Buck-1, uses partial charges and the second, Buck-2, uses nominal charges.^{42–44} The list of parameters is given in Table I. In the case of Buck-1, r_0 values are not reported by the authors, so we have used the Newton–Raphson method to find them. In the case of Buck-2, we have found B_{ij} , D_{ij} , and n by requiring that the two potential functions and their first and second derivatives at the distance r_0 be matched. The implementation is done by constructing tabulated potentials for the LAMMPS library package,^{45,46} which is used as the force-calculation engine and is linked to our k-ART code (see the [supplementary material](#) for details on table constructions and their LAMMPS implementation). The cutoff distance for computing long-range interactions into the k -space is set to $r_c = 16$ Å; lower values show problems of convergence or do not recover the spinel structure. The precision for Buckingham is set to $\epsilon = 10^{-10}$ with the Ewald method.

III. RESULTS AND DISCUSSION

A. Basic predictions in a normal spinel

Both Buck-1 and Buck-2 correctly predict the geometry at zero pressure, with a lattice constant a of 8.606 Å and 8.415 Å, respectively, whereas the experimental value is 8.339 Å. The bulk modulus is 164.57 GPa (Buck-1) and 223.25 GPa (Buck-2), whereas the experiment predicts 198.2 GPa. Both potentials predict larger anion parameters of 0.385 and 0.388, respectively (the ideal anion parameter is $u_{43m} = 0.375$), which has an effect on the diffusion pathways due to changes in anion–cation distances. Other properties of a perfect spinel crystal using these potentials, such as elastic constants,

shear and Young’s moduli, and cohesive energy, have been discussed previously in Ref. 39.

B. Vacancy and interstitial formation energies of the symmetric equipoints

It is interesting to first observe the predictions under lattice symmetries when defects are formed. For a monatomic system, the defect formation energy can be computed using the following well-known formula:

$$E_{v,int} = E'_t - \frac{N \pm n}{N} E_t, \quad (4)$$

where the minus sign is for a vacancy, E_v , and the plus sign for an interstitial, E_{int} . E'_t is the energy computed after removing or adding n defects and relaxation of the crystal, and E_t is the total energy of a perfect crystal with N atoms also obtained after relaxation of the system. However, in a ternary system, there are three different types of atoms that contribute with different fractions to the energy, so the formation energy of n defects is redefined as

$$E_{v,int} = E'_t - \frac{N_1 \pm n}{N_1} E_{t1} - E_{t2} - E_{t3} = (E'_t - E_t) \pm \frac{n}{N_1} E_{t1}, \quad (5)$$

where E'_t is the energy computed after creating a defect of type 1 and relaxation of the crystal, E_{ti} are the total energies by ion type i in the perfect crystal, and N_1 is the number of ions of type 1 where the defects are created, with $E_t = E_{t1} + E_{t2} + E_{t3}$ being the total energy of the perfect crystal and $N = N_1 + N_2 + N_3$.

Since changing the box size means changing the vacancy concentration, here we do calculations as a function of the box size k (supercell $k \times k \times k$ unit cells), the plots are shown in Fig. 2. We see that as the box size increases, E_v converges to a fixed value, so we fit to a Debye type formula,

$$D_v(k) = \frac{ce^{-bk}}{1 - e^{-bk}} + E_v, \quad (6)$$

where b , c , and E_v are the fitting parameters, and in the limit when k is infinite, the vacancy formation energy is obtained as the last

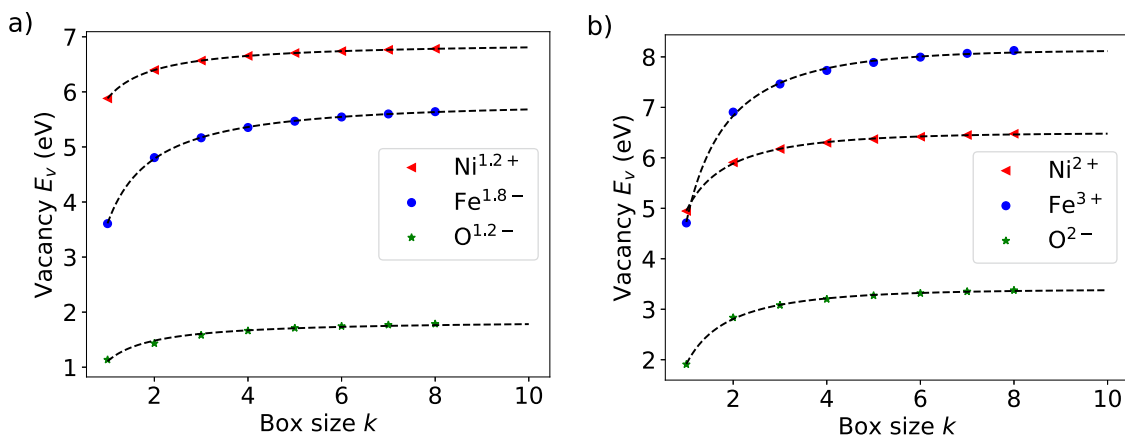


FIG. 2. Vacancy formation energies in normal-spinel structures of NFO. (a) Buck-1 and (b) Buck-2. The dashed lines are plots of Eq. (6), fitted to the data. Only one vacancy ($n = 1$) per value of k .

TABLE II. Fitted vacancy formation energies (eV) in normal-spinel structures of NFO.

Vacancy	Ni	Fe	O
DFT ($1 \times 1 \times 1$) ^{47,48}	0.52	1.56	2.87
Buck-1 (fitting)	5.04	6.57	2.34
Buck-2 (fitting)	6.49	8.13	3.39

term E_v . The fitting results are given in Table II. It shows that the energies required to form vacancies are high, suggesting that high temperatures are required to create them. While the O vacancy formation energies of 2.33 eV (Buck-1) and 3.39 eV (Buck-2) are quite close to the DFT results (2.87 eV), the calculated formation energies for Fe and Ni vacancies, although of the same order ($E_v^{\text{Ni}} < E_v^{\text{Fe}}$), are many eV's larger than the DFT results.^{47,48} This means that, contrary to DFT, for Buck-1 and Buck-2, O vacancy should form preferably to metallic vacancies. Two reasons might explain this difference: (i) the simulation cell: in the DFT calculations, a primitive unit cell box was used,^{47,48} which may be not large enough to prevent interaction of the vacancy with itself because of the periodic boundary conditions, and (ii) the nature of the charged defect: in DFT, the vacancy formation energy is calculated by $E_v = (E'_i - E_i) + E_X$, where E_X is the energy of an ion X obtained from its pure crystal of fcc Ni or bcc Fe, and for O, half the energy of the O₂ molecule: $\frac{1}{2}E(\text{O}_2)$,⁴⁹ so E_X can be interpreted as the chemical potential of ion X.⁵⁰ In our case, E_X cannot be calculated directly from a reference structure because cations have only repulsive terms, but it is noted that $E_X \approx E_{i1}/N_1$, which here is taken according to the spinel structure.

The interstitial formation energies for Buck-1 and Buck-2 are calculated only at a concentration of one ion per $2 \times 2 \times 2$ box due to the number of sites, although it is expected that these energies will have a similar behavior with box size as shown in Fig. 2. The results are given in Table III, depending on the exact equipoint used, namely 8b, 16c, and 48f. We also analyze the final

energies after relaxation of these interstitial equipoints. In this case, according to formula (5), the chemical potential for an interstitial is approximately $E_X \approx -E_{i1}/N_1$.

Despite the lattice symmetries of the ideal spinel cell, the landscapes of Buck-1 and Buck-2 are rough. There are also some discrepancies between the predictions of the two potentials, although both agree that the lowest energy relaxation of Ni is in an octahedron 16c and that of Fe is in a tetrahedron 8a, while 8b and 48f are metastable sites with relaxation depending on the exact initial point within the tetrahedrons. In the case of the 8b equipoint, Buck-1 relaxes Ni to 8b and Buck-2 relaxes Ni to 16c (so 8b is a metastable point), while Buck-1 relaxes Fe to the 16c point and Buck-2 relaxes Fe to a metastable point at the interface between two octahedral and tetrahedral sites. More interesting is the case of interstitial cations initially located at the tetrahedral points of the 48f equipoint, where the final relaxation point depends on the exact initial location of the interstitial within this octahedral site. For cations (Ni or Fe), relaxation can be made directly to the 16c point, or a displacement of the nearest Ni at an 8a site to a 16c site and the occupation of the 8a site by the interstitial (in the case of Ni, note that the energies are the same as the final configurations are equivalent). Energy relation following the insertion of an O interstitial at any of the equipoints leads to a local disordered structure, and for 48f, three final configurations are predicted.

The formation energies correspond to the final relaxation points, and both potentials predict that, in contrast to the vacancy formation energies, the O interstitial is the most difficult to form with formation energies around 8 eV, which is high. In contrast, Buck-1 predicts that a Ni interstitial is the easiest to form (except at 8b, which requires ~8.6 eV to form), whereas Buck-2 predicts that Fe is the easiest to form. Unfortunately, we do not find any experimental or DFT results to compare. This may be because it is already known that these equipoints are thermodynamically unstable due to the shorter central ionic distances and the increased electrostatic repulsion.⁵¹ However, these sites can participate in the diffusion pathways as shown in Secs. III C and III D.

TABLE III. Minimum energies E'_i (eV) and their relaxation sites; the last three columns are interstitial formation energies E_{int} (eV). The perfect crystal energies are $E_i = -4857.781$ eV (Buck-1) and $E_i = -12382.319$ eV (Buck-2).

Buck-1	E'_i Ni	E'_i Fe	E'_i O	E_{int} Ni	E_{int} Fe	E_{int} O
8b	-4858.1978b	-4873.28316c	-4858.175	8.626	1.421	7.859
16c	-4866.21016c	-4873.28316c	-4858.175	0.613	1.421	8.357
	-4866.21016c	-4873.28316c	-4858.175	0.613	1.421	7.859
48f	-4866.2108a	-4873.9528a	-4858.665	0.613	0.752	7.370
	-4866.2108a	-4873.9528a	-4858.170	0.613	0.752	7.865
Buck-2						
8b	-12400.26216c	-12420.263 ^a	-12394.783	3.156	6.706	8.305
16c	-12399.94816c	-12423.23116c	-12394.783	3.469	3.738	8.305
	-12399.94816c	-12423.23116c	-12394.783	3.469	2.891	8.305
48f	-12399.9488a	-12425.6768a	-12394.640	3.469	1.293	8.449
	-12399.9488a	-12425.6768a	-12395.324	3.469	1.293	7.764

^aMetastable minimum. Relaxation of Fe is to interface between two octahedral and tetrahedral sites.

C. Vacancy diffusion mechanisms

Simulations of k-ART with Buck-1 and Buck-2 parameterizations were run with three vacancy types: Ni, Fe, and O. A vacancy was randomly located in the sample, and the temperature was set to 300 K for all simulations presented here and up to 1000 steps. The simulations run for 15–20 days each using 8–16 cores per run.

The generated event catalogs contain relevant information about the diffusion mechanisms, as each different mechanism is associated with a unique topological key. On average, k-ART has found $\sim 10^3$ topologies per simulation, most of them are closely related structures differing by small geometric deformations as shown, for example, by the small number of different barrier energies. Figure 3 reports barriers E_b vs the inverse barriers, i.e., barriers crossed to get back to previous states, $E_{inv} = E_{saddle} - E_{new}$, and barriers vs displacements, Δr , given by the root of Eq. (1). From these plots, we see that for many events, the inverse barriers E_{inv} are proportional to E_b and, in the case of Ni, $E_{inv} \approx E_b$, so there is some symmetry between the initial and final states. However, we also observe that saddles are not always at the geometric middle point of the path, i.e., many events do not have such a symmetry in their path. This could suggest that there are many diffusion mechanism families. However, a closer analysis of their geometric nature shows that many of them are very similar, i.e., there are only small variations in the coordinates, so it is possible to reduce these families to a few (5–10). Only one or two of these families dominate vacancy

diffusion at 300 K; these selected mechanisms are described in detail in the following discussion.

For the Ni vacancy, Buck-1 predicts a diffusion coefficient of $D \sim 1.4 \times 10^{-13}$ m²/s at 300 K with alternating barrier energies of 0.17 and 0.36 eV. The path is shown in Fig. 4 where Ni vacancy diffusion from one site to the same in the adjacent cell occurs in five steps: an adjacent Ni ion jumps to a saddle point (octahedral–tetrahedral interface), then relaxes to an octahedral minimum 16c, after which it jumps to a symmetric second saddle point, and finally relaxes to the octahedral vacancy. By comparing to Fig. 1, the Ni vacancy path is 8a to 8a via 16c. This migration mechanism has already been observed in the diffusion of Mg ions in MgMnCrO₄ spinel, which is useful for cathodes in rechargeable Mg-ion batteries.⁵²

Buck-2 predicts the same geometric path as Buck-1, but without an intermediate saddle point split, so the saddle point is just the octahedral site. The unique barrier is at 0.87 eV, which is more than double that obtained with Buck-1. Therefore, the diffusion coefficient at 300 K is reduced to $D \sim 5 \times 10^{-22}$ m²/s, corresponding to jumps taking place every 100 s, on average, implying that Ni vacancies are very stable in time at 300 K.

In the case of Fe vacancy, Buck-1 predicts a diffusion coefficient of $D \sim 7 \times 10^{-20}$ m²/s and movement is in two steps with barrier energies of 0.32 and 0.74 eV. Thus, vacancy diffusion at 300 K is slow, with large time steps of up to 10⁴ s (a few hours). Similar to Ni vacancy, the diffusion path for Fe vacancy occurs in five

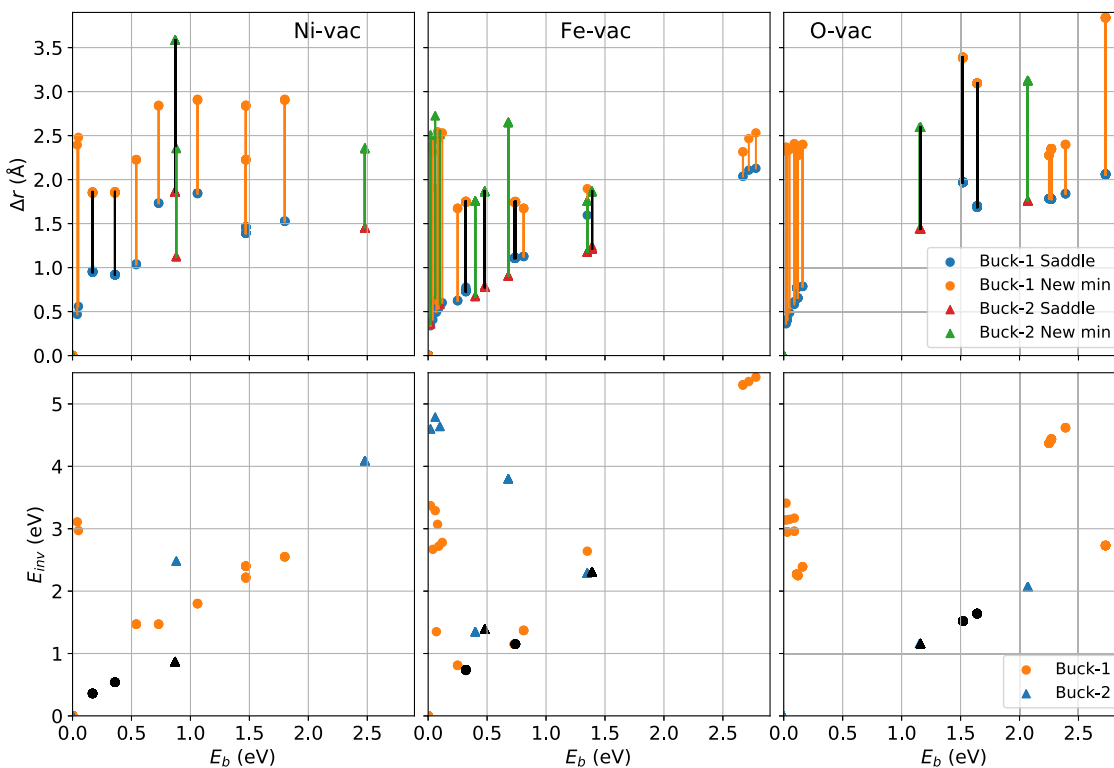


FIG. 3. Vacancy diffusion: displacements, barriers, and inverse barriers for events found in the k-ART-generated catalog. Displacements from saddles to final minima are connected by lines (all displacements are measured from initial minima). In black, barriers and displacements that allow diffusion at 300 K.

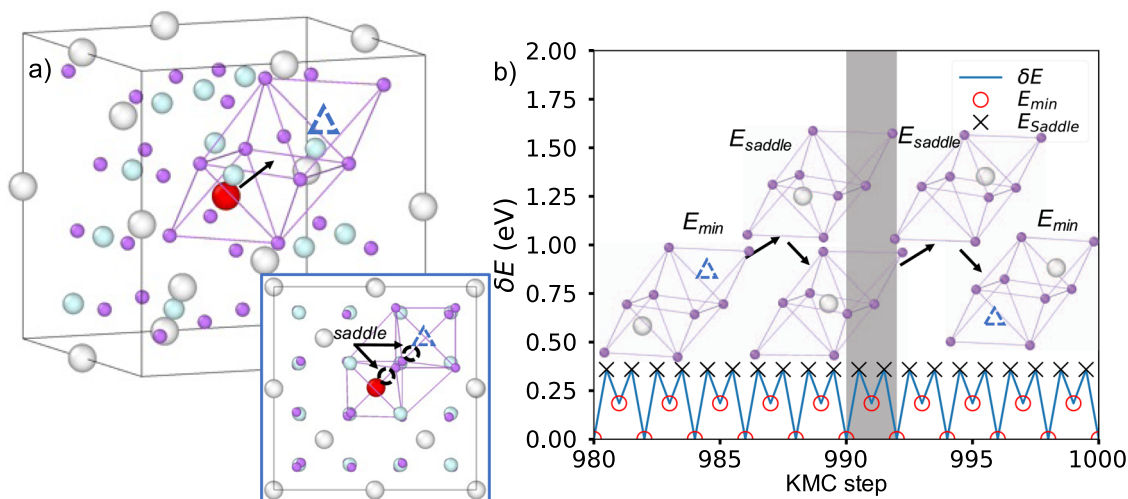


FIG. 4. Ni vacancy diffusion by Buck-1. (a) 3D and top views of the unit cell; gray spheres represent Ni, blue spheres represent Fe, purple spheres represent O, and red spheres are atoms that allow Ni vacancy diffusion. (b) Change in energy as a function of the KMC steps; the inset images show the geometry of the Ni vacancy diffusion, the dashed triangles represent a tetrahedral vacancy, the black crosses are maximum energies, and the red circles are minimum energies. The gray band represents an event.

steps: it starts with a jump of a Fe ion from one octahedral site to another adjacent octahedral site via a connecting tetrahedral site at a higher energy, as described in Fig. 5. The symmetrical saddles are at the octahedral and tetrahedral interfaces. The path is not unique, as each tetrahedron is connected to four octahedrons, all with the same probability of being chosen. As for Ni vacancies, Fe vacancies have long resident times. Buck-2 recovers the same path as Buck-1, including the two-step saddle point, but with higher barrier energies: 0.48 and 1.39 eV; the diffusion coefficient in this case is $D \sim 4 \times 10^{-31} \text{ m}^2/\text{s}$. Comparing to Fig. 1, the Fe vacancy path is

16d to 16d via 48f, in agreement with Sickafus as mentioned in the Introduction.²²

The diffusion mechanism of O vacancies is described in Fig. 6 with Buck-1. The geometry around the vacancy shows that the nearest O-ions form the corners of a cuboctahedron, with the vacancy in the center. An O-ion then jumps from one of the corners to the saddle in a square plane (see the inset images in Fig. 6) and finally to the vacancy at the center. Due to large 1.52 eV barrier energies, the O vacancy diffusion has a long resident time with time steps of up to 10^{18} s (billions of years) at 300 K, with a diffusion

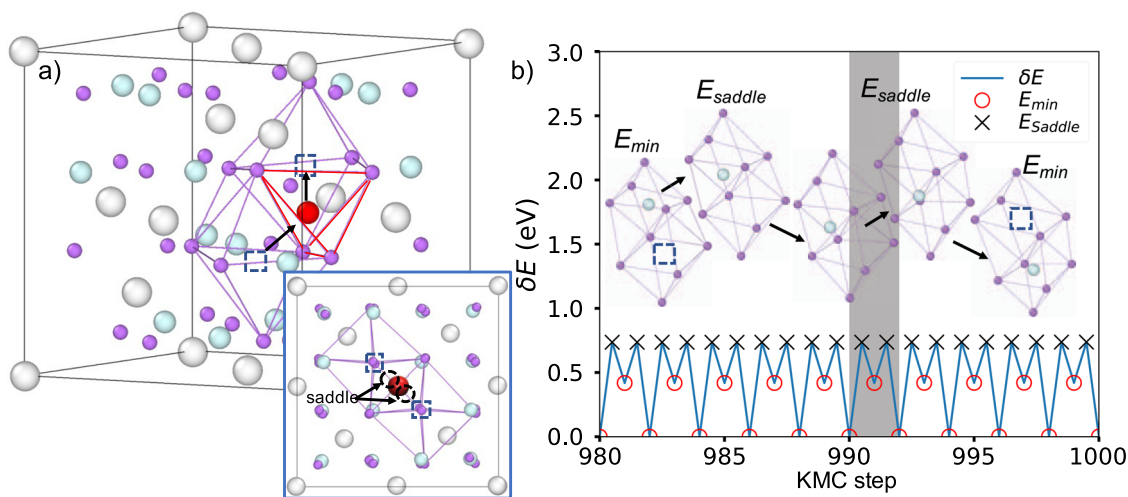


FIG. 5. Fe vacancy diffusion by Buck-1. (a) 3D and top views of the unit cell. (b) Change in energy as a function of the KMC steps. The inset images show the geometry of the Fe vacancy diffusion, the dashed squares represent the octahedral vacancy, and the dashed circles represent the saddles.

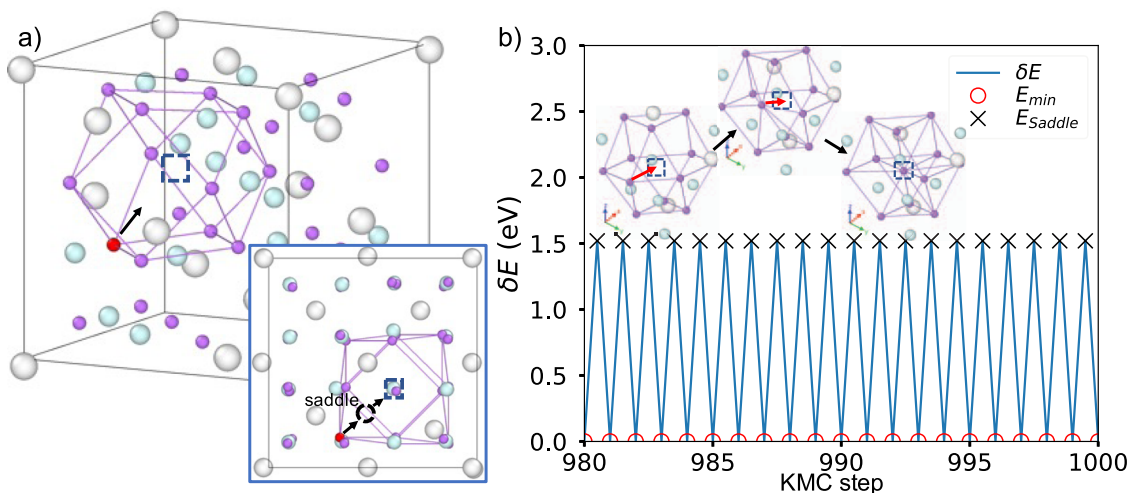


FIG. 6. O vacancy diffusion by Buck-1 in a cuboctahedron. (a) Unit cell view and (b) the change in energy as a function of the KMC steps. The inset images show the geometry of the O vacancy diffusion, and the dashed square represents the O vacancy. In red, an O ion at the saddle point and moving to the adjacent O vacancy.

coefficient with Buck-1 of $D \sim 10^{-32} \text{ m}^2/\text{s}$. A second mechanism for O-vacancy diffusion, with a barrier energy of 1.63 eV that includes an additional displacement of a Ni-ion, is also found; this event only occurs 4 times in 1000 steps.

Because the cuboctahedron has 8 triangular faces and 6 square faces with O-ions at the vertices, it is radially equilateral, so all O-ions should have the same probability of occupying the O vacancy in the center. The square displacement for the O vacancy with Buck-1 is shown in Fig. 7 together with the number of topologies found. Although more than 800 different topologies are found by k-ART, after careful analysis, we find that most of these topologies correspond to the same class of mechanisms, with the difference linked to a relatively flat energy surface near the saddle. At 300 K, one barrier dominates and the plot of the square displacement is almost a straight line.

Although this simulation reached 1000 steps, a clear O vacancy diffusion with the Buck-2 potential was not observed as the system was trapped in a basin. Nevertheless, the analysis of the event catalogs shows that the Buck-2 potential produces the same mechanisms as Buck-1, but with a barrier energy of 1.16 eV instead of 1.52 eV of Buck-1.

D. Interstitial diffusion mechanisms

We now proceed with the discussion of the diffusion of the interstitials as these mechanisms are very important for understanding many practical applications of spinels. As before, only a normal spinel $2 \times 2 \times 2$ box is considered. In all simulations and for each potential, the box is set to zero pressure with LAMMPS; then, an interstitial ion is randomly placed, and the energy of the

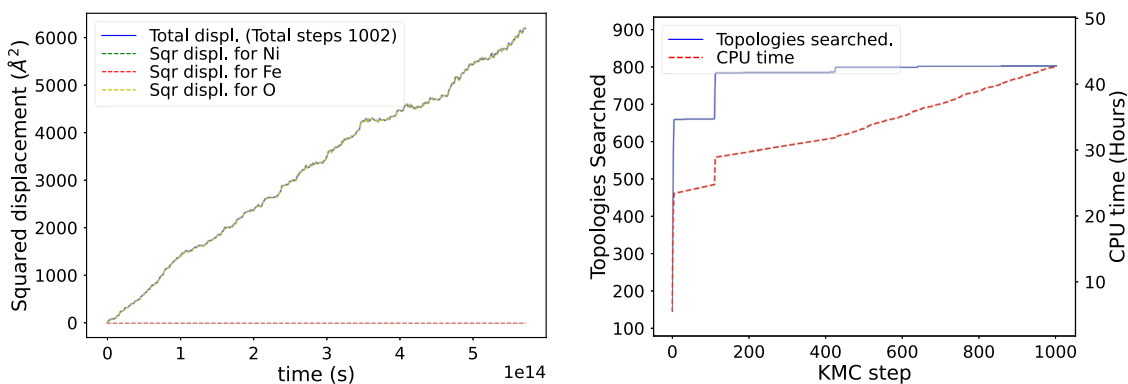


FIG. 7. On the left, square displacement vs time (time multiplied by 10^{14}), only O diffuses. On the right, the number of topologies found during the simulations and the CPU time consumed.

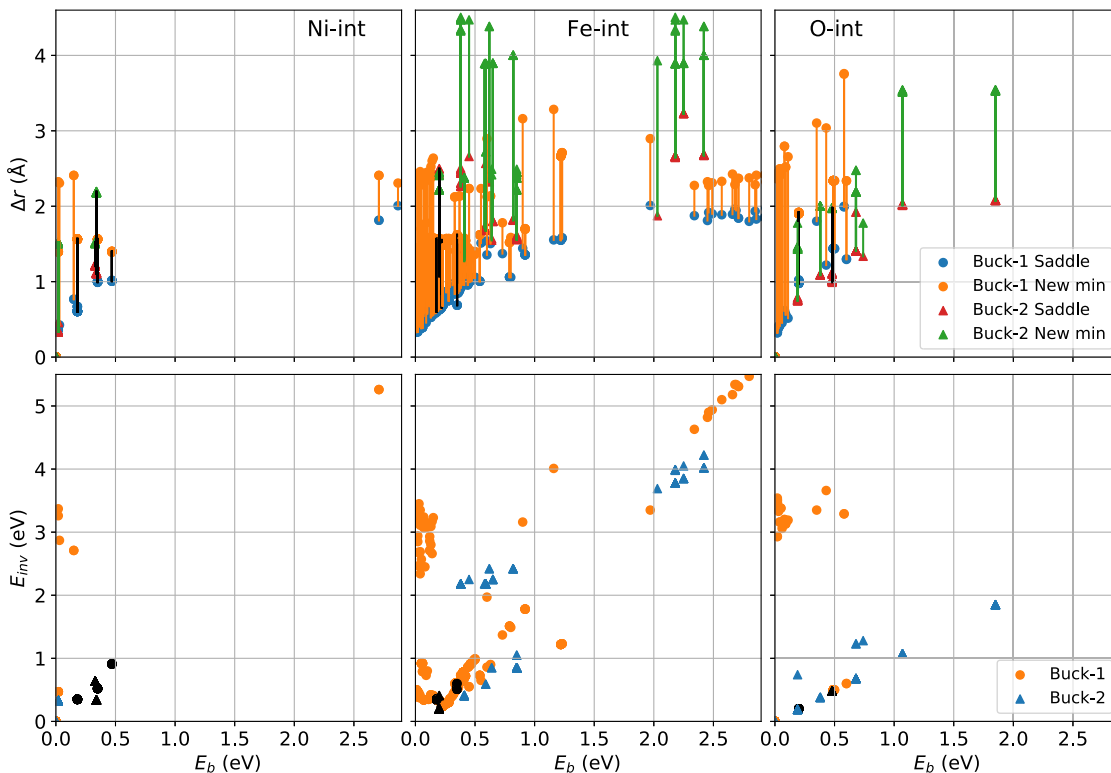


FIG. 8. Interstitial diffusion: k-ART predictions of displacements, barriers, and inverse barriers for events found in the catalog. Distances from saddles to new minima are connected by lines (distances from old minima to new minima must be taken from zero). In black, barriers and displacements that allow diffusion at 300 K.

system is relaxed before starting the KMC steps. Figure 8 shows the predicted barriers and displacements by k-ART for interstitial diffusion. Again, we observe a wealth of mechanisms and, similar to vacancies, only one or two events dominate the kinetics of the

diffusion at 300 K. Moreover, while the two potentials seem to predict many different mechanisms, a closer inspection reveals that many of them are similar (similar paths with different barriers). There are also too many states that may conduit to flickering states,

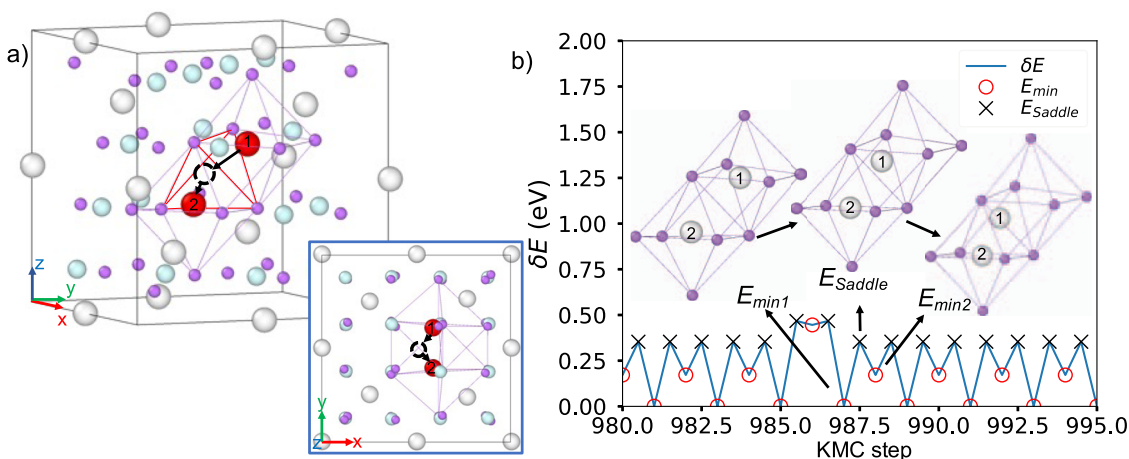


FIG. 9. Ni interstitial. (a) 3D and top views along the (100)-direction of the ground state; origin translated by half lattice in each direction with respect to Fig. 1. Gray spheres represent Ni, blue spheres represent Fe, purple spheres represent O, red spheres are the diffusing Ni ions at 16c sites, and the dashed circle is an 8a site. (b) Energy changes when jumping from one minimum to another via the saddle point as shown in the inset.

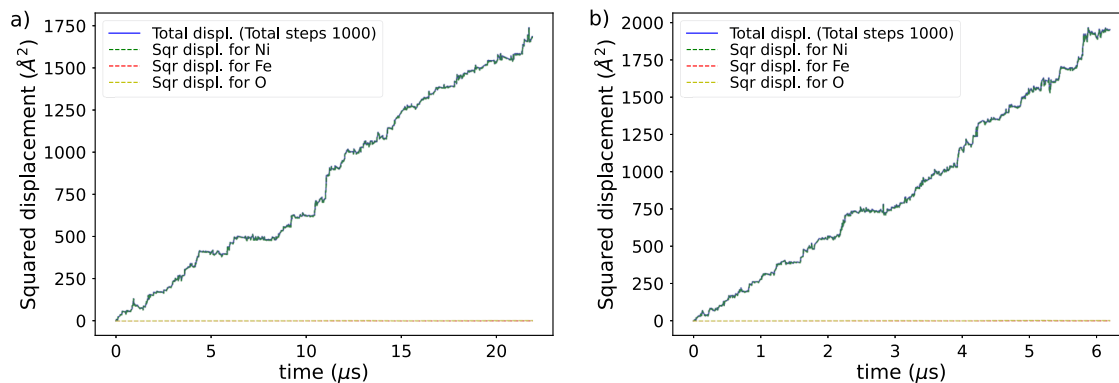


FIG. 10. Squared displacement of the Fe and Ni ions using (a) Buck-1 and (b) Buck-2. Fe does not diffuse but only provides the mechanism to trigger the Ni diffusion.

which are correctly handled by the bac-MRM method during the KMC steps.

Figure 9 describes the Ni-interstitial diffusion mechanism with Buck-1: in panel (a), the ground state and diffusion pathway are indicated by arrows, and in panel (b), the energy changes when jumping (only half the path is shown because of symmetry). Diffusion occurs through five steps (including saddles) and involves two Ni ions: After relaxation of Ni1 interstitial to an octahedral 16c metastable minimum [$E_{\min 2}$ in Figure 9(b)], a nearest Ni2 ion at 8a site jumps to the nearest empty octahedral 16c site, thus arriving at the ground state [$E_{\min 1}$ in Fig. 9(b)]; saddles are when a Ni is at the interface between the octahedral and tetrahedral sites [E_{saddle} in Fig. 9(b)]. The cycle finishes with Ni1 jumping to the 8a site ($E_{\min 2}$ configuration). The 300 K diffusion coefficient is $D \sim 6.4 \times 10^{-14} \text{ m}^2/\text{s}$ with barrier energies of 0.35 eV and then 0.18 eV and for some events with barrier energies of 0.47 eV and then 0.02 eV [see Fig. 10(a)], but the mechanism is the same; this later seems to be an artifact of the potential. Note that octahedral points such as 8b or 48f are not involved in diffusion. There is also a larger barrier at step 986 of the same path; this

barrier appears to be an artifact of the potential created by a third Ni ion jumping out of its cell position.

Buck-2 predicts the same overall diffusion path as Buck-1 for a Ni-interstitial, but, for some steps, a metastable intermediate minimum corresponding to a stretched saddle point is found. In this case, the diffusion coefficient is $D \sim 2.4 \times 10^{-13} \text{ m}^2/\text{s}$ with a barrier energy of 0.34 eV and for some events via an intermediate step with a barrier energy of 0.02 eV [see Fig. 10(b)], although the total path is the same.

Although the mechanism for Fe jumping from the 16c site to the 16c site is predicted with a barrier energy of 0.54 eV (similar to Ni diffusion, the nearest Ni at the 8a site must first move to the 16c site) with Buck-1, Fe-interstitial diffusion is not observed, rather we find one of the most surprising mechanisms in spinel diffusion: it is the one by which Fe-interstitial triggers Ni diffusion. More precisely, the Fe-interstitial relaxes to an energy minimum in an octahedral site 16c and then jumps in a series of steps to a tetrahedral site 8a occupied by Ni, displacing the Ni-ion to an interstitial octahedral 16c site and triggering Ni diffusion. Figure 11(a) describes

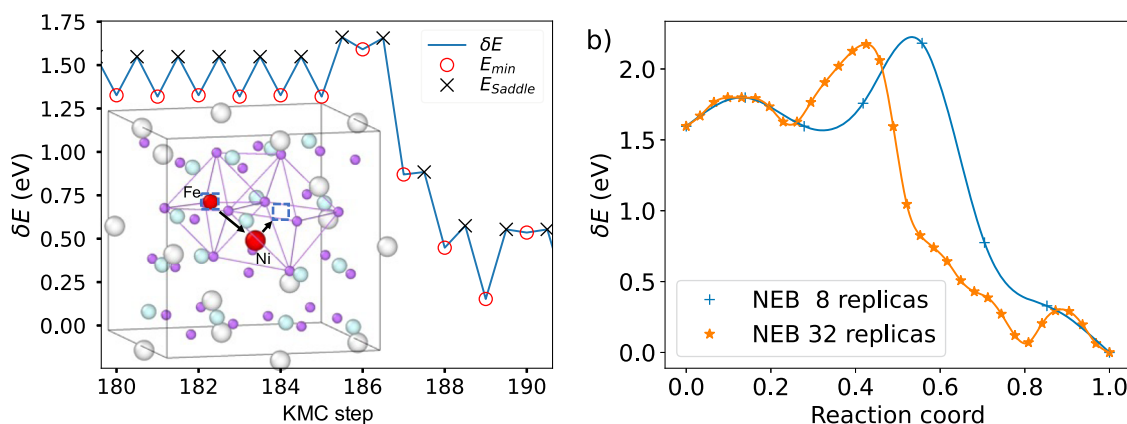


FIG. 11. Diffusion of the Fe interstitial. (a) The activation energies for Ni ion diffusion with Buck-1; the interstitial Fe takes the place of Ni, stabilizing at the tetrahedral site, so that Ni starts to diffuse (see the inset images). (b) CI-NEB results for Buck-2 using 8 and 32 replicas for a better path resolution.

this activation mechanism, which occurs with a barrier energy of 0.34 eV (activation of migration of Fe interstitial from octahedral to tetrahedral sites) and migration of Ni with 0.18 and 0.35 eV Ni diffusion (same as in Fig. 9); the inverse barrier is 1.50 eV. A barrier energy observed of ~ 0.22 eV is also observed, but it leads to flicker states. This mechanism can explain how Fe-interstitials contribute to the formation of inverse spinels, the most common NFO spinel structure. Therefore, once the Fe ion displaces the Ni ion, a large barrier energy of 1.50 eV is required for Fe diffusion, as opposed to the 0.35 eV barrier energy required for Ni diffusion.

Due to problems with the roughness of the potential, creating KMC diffusion pathways for a Fe interstitial was not possible with the Buck-2 parameters. However, since the initial and final states are already known from Buck-1 and well reproduced by Buck-2, we use the CI-NEB method to obtain the main barrier and inverse barrier, with an energy of 0.59 and 2.18 eV, respectively [see Fig. 11(b)], giving a 1.6 eV difference between the initial and final states. These results are in good agreement with previous results for Buck-1. We also observe two other peaks with a barrier and an inverse barrier of 0.20/0.20 and 0.22/0.29 eV, respectively, which represent intermediate steps similar to those found with Buck-1. Similar to Buck-1, once the Fe ion displaces the Ni ion, a large barrier of 2.18 eV is required for Fe diffusion, as opposed to the 0.34 eV barrier energy required for Ni diffusion with Buck-2.

The diffusion mechanism of an O interstitial is another one of the most interesting mechanisms found in this work. The insertion of an O interstitial ion triggers diffusion of several O ions, all moving in the same line, as described in Fig. 12. Both potentials, Buck-1 and Buck-2, identify the same collective mechanism. In these figures, the O ions involved in diffusion are surrounded by red circles and the green circle shows the deformation area centered in the O interstitial. As explained above, relaxing the O interstitial leads to a distorted structure that breaks local symmetries. This collective disordering is not expected and could not easily be predicted with two-ended methods such as CI-NEB.²⁶

Using the Buck-1 parameterization, 1291 KMC steps were reached, predicting an O diffusion coefficient of $D \sim 8.9 \times 10^{-13}$ m²/s and a unique migration barrier energy of 0.20 eV. With Buck-2, the predicted diffusion coefficient was $D \sim 1.5 \times 10^{-17}$ m²/s over 1000 KMC steps (or in another run, $D \sim 8.6 \times 10^{-17}$ m²/s). In this case, the collective movement was triggered by initial barrier energies of 0.19 and 0.14 eV after initial relaxation of the O interstitial, so the O collective diffusion occurred with a total barrier energy of 0.48 eV.

Figure 13 shows the square displacement as a function of time for a group of O ions induced by the O interstitial introduced, as recovered by both Buck-1 and Buck-2 parameterizations. Although a clear non-zero slope is not observed in the first steps of Fig. 13, dif-

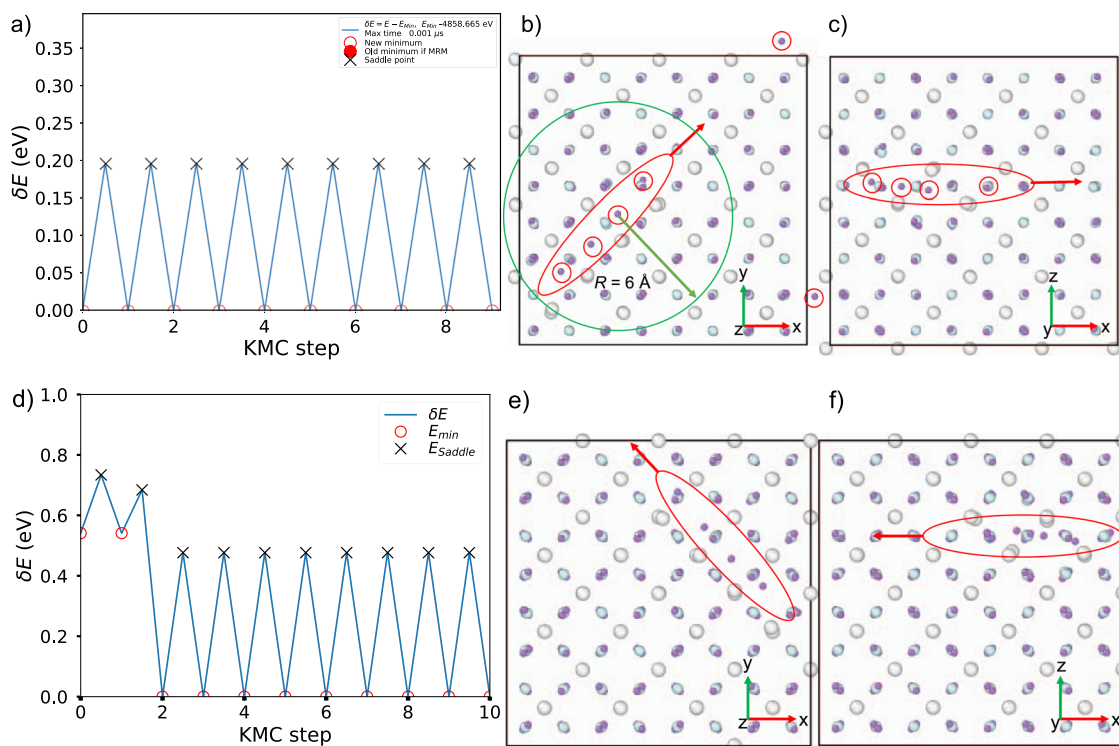


FIG. 12. Collective diffusion of O-ions in a spinel induced by an O-interstitial. Buck-1: (a) Barrier energies as a function of steps. (b) and (c) Images of the xy and xz planes. Diffusing atoms are encircled, and the red arrows indicate the direction of diffusion. The green circle is the topological region selected in k-ART.

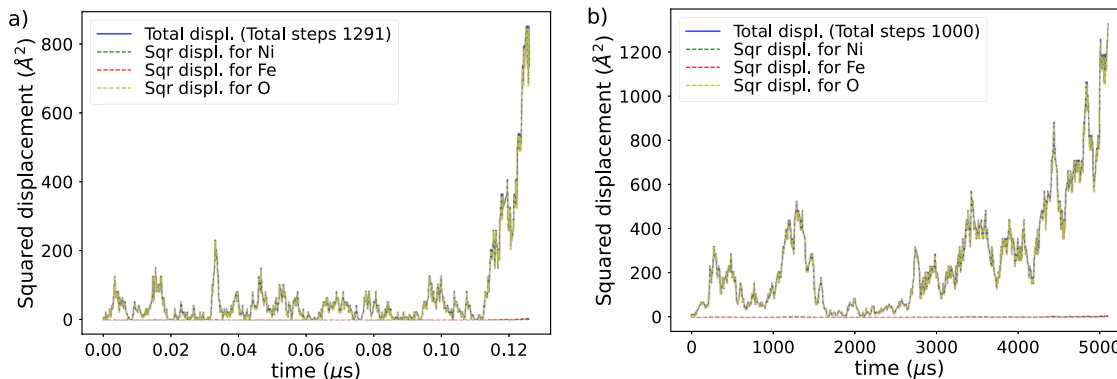


FIG. 13. Square displacement of the collective diffusion of O ions with (a) Buck-1 and (b) Buck-2 induced by an O interstitial. Barrier energies of 0.2 and 0.48 eV [see Figs. 12(a)–12(d)] are responsible for the 10^5 time difference.

TABLE IV. Summary of estimated diffusion coefficients D (m^2/s) for a NFO normal spinel at 300 K found in simulations and their total effective barrier energies E_b (eV) between two minima.

Vacancy	Ni		Fe		O	
	D	E_b	D	E_b	D	E_b
Buck-1, normal	1×10^{-13}	0.36	7×10^{-20}	0.74	1×10^{-32}	1.52
Buck-2, normal	5×10^{-22}	0.87	4×10^{-31}	1.39	...	1.16
DFT, inverse ¹²	...	1.21	...	0.7
Interstitial	D	E_b	D	E_b	D	E_b
Buck-1, normal	6×10^{-14}	0.35	9×10^{-13}	0.20
Buck-2, normal	2×10^{-13}	0.34	1×10^{-17}	0.48/0.19
DFT, inverse ¹²	...	1.40	...	1.00

fusion does take place in the end, as confirmed by the animation of the corresponding coordinates. Both catalogs (Buck-1 and Buck-2) do indeed suggest many other mechanisms for O interstitial diffusion, as observed in Fig. 3 and Fig. 8, some of which are similar to those that could be predicted using two-ended methods such as CI-NEB. Such symmetric pathways are not the most probable according to our k-ART simulations, however. The observed 10^5 time difference scale is due to the barrier energies of 0.2 and 0.48 eV for Buck-1 and Buck-2, respectively [see Figs. 12(a)–12(d)].

Table IV summarizes the calculated values of the diffusion coefficients and their total effective barrier energies. It should be emphasized that data on Fe interstitial diffusion are not included because Ni diffusion occurs instead, as previously explained in Fig. 11. Table IV also shows the DFT predicted migration barrier energies for the cation vacancy and the interstitial in an inverse spinel.¹² These DFT results show a strong site preference for cation vacancies to occupy the octahedral sites, whereas the equilibrium concentration of tetrahedral site vacancies is predicted to be extremely low, so the hops are octahedral–octahedral.¹² However, care must be taken as there is no direct comparison with normal spinel mechanisms. More importantly, previous MD work predicts that in inverse spinel systems, the stresses produced by the randomization of the

octahedral sites can cause vacancy formation energy fluctuations of up to 35% for cations and up to 71% for anions with respect to their means.⁵³ Thus, a similar behavior is expected for the calculation of energy barriers largely affecting the diffusion mechanisms. We do not calculate here the diffusion mechanisms in an inverse spinel, as a statistical study is required; this study is reserved for future work.

Finally, we see that the diffusion coefficients differ by orders of magnitude when comparing both potentials for the same element, this is a consequence of the difference in barrier energies, time changes exponentially with barrier energies, and by Eq. (2), the diffusion coefficient is proportional to time, so slower barrier means faster diffusion.

IV. CONCLUSIONS

Diffusion mechanisms in normal spinel ferrites NiFe_2O_4 have been studied using two different Buckingham potential parameterizations: one with partial charges, Buck-1, and the other with full charges, Buck-2. Although both potentials predict an abundance of events per defect, both parameterizations predict the same diffusion mechanisms at 300 K when the total path is considered. While predicted barrier energies differ depending on the potential used,

of the three ions, Ni systematically diffuses the fastest. In terms of potentials, the use of full charges, as is the case for Buck-2, makes the diffusion of anions more difficult because of the higher barriers predicted and thus the lower diffusion coefficients. It, however, facilitates the diffusion of cations because of the predicted lower barriers.

The vacancy diffusion mechanisms found by k-ART correspond to those expected from previous studies,^{15,16,22} although there are many other events that could be selected at other temperatures. In general, we have found that vacancies are stable (long residence times), so their diffusion is slow. Resuming the mechanisms, we find that the Ni vacancy diffusion happens in three steps using an octahedral site as a saddle point with a total barrier energy of 0.36 eV Buck-1 or 0.87 eV Buck-2. The Fe vacancy diffusion takes place in five steps using two octahedral sites connected by a tetrahedral site with a total barrier energy of 0.74 Buck-1 or 1.39 eV Buck-2. The O vacancy is centered by 12 O ions forming a cuboctahedron, and O ions at the corners can jump to the center with a barrier energy of 1.52 eV Buck-1 or 1.16 eV Buck-2. We conclude that the change from normal to partial charges only affects the barrier energies predicted by Buckingham potentials, but the paths remain the same.

In contrast, unexpected mechanisms are found for the diffusion of Ni, Fe, and O interstitials at 300 K. We conclude that the excess of Fe interstitials leads to the formation of partial inverse spinels. These mechanisms contrast with what is intuitively expected, where one would expect the exchange of Ni and Fe ions between tetrahedral and octahedral sites, activated at a certain temperature; however, these mechanisms are not observed due to very large barriers that are difficult to generate in a $2 \times 2 \times 2$ cell.

It is also very interesting to note that intuitive mechanisms such as interstitial ions jumping from octahedral site 16c to 16c via tetrahedral site 48f, as found by DFT using CI-NEB,¹² are not selected by k-ART at 300 K. This notable difference could be due to our use of open-ended search approach (ARTn) for transitions. Furthermore, the tetrahedral points 8b and 48f, which can be intuitively considered as saddle points, are not used as the preferred pathway for interstitial diffusion in NFO according to our study. It is also worth noting that the ground state is not the one with a Ni (or Fe) interstitial at octahedral 16c; although this minimum exists, it is metastable. For a Ni interstitial, the ground state occurs when the nearest Ni at 8a jumps to the nearest 16c site, so the ground state is formed by two Ni ions at 16c sites. In the case of Fe, although the configuration with Ni and Fe located at two adjacent octahedral 16c sites has lower energy, the ground state is when Fe is located at a tetrahedral 8a site and displaced Ni at an octahedral 16c site.

The excess of O interstitials also leads to collective O diffusion, a mechanism that cannot be predicted intuitively, as one usually only suspects that an atom jumps between two minima by crossing a desired barrier. We emphasize that the same mechanisms are observed in Buck-1 and Buck-2.

Finally, although we found no experimental or DFT results for the interstitial migration barriers in a normal spinel NFO, we did find results for the inverse structure. This is expected as the normal phase is never observed experimentally, but working here with a normal NFO has helped us understand why the normal phase is never observed. Ideally, simulations should be performed using inverse spinel structures and considering the inversion parameter as

a key factor, but due to the complexity of the generated events, we do not address such types of simulations, which could be considered in future work.

SUPPLEMENTARY MATERIAL

The [supplementary material](#) contains implementation details of the tabulated potentials used here and minimal LAMMPS scripts.

ACKNOWLEDGMENTS

N.M. acknowledges the partial support by a Discovery grant from the Natural Sciences and Engineering Research Council of Canada (NSERC). We acknowledge the Calcul Québec/Digital Research Alliance of Canada (CQ/DRAC) for generous allocations of computer resources. The k-ART package is available for distribution by contacting the authors.

AUTHOR DECLARATIONS

Conflict of Interest

The authors have no conflicts to disclose.

Author Contributions

Oscar A. Restrepo: Conceptualization (equal); Data curation (equal); Formal analysis (equal); Funding acquisition (equal); Investigation (equal); Methodology (equal); Project administration (equal); Validation (equal); Visualization (equal); Writing – original draft (equal); Writing – review & editing (equal). **Charlotte S. Becquart:** Investigation (equal); Validation (equal); Writing – review & editing (equal). **Normand Mousseau:** Investigation (equal); Resources (equal); Software (equal); Validation (equal); Writing – review & editing (equal).

DATA AVAILABILITY

The data that support the findings of this study are available within the article and its [supplementary material](#).

REFERENCES

- ¹A. Polo, C. R. Lhermitte, M. V. Dozzi, E. Selli, and K. Sivula, “Hydrogenation of ZnFe₂O₄ flat films: Effects of the pre-annealing temperature on the photoanodes efficiency for water oxidation,” *Surfaces* **3**, 93–104 (2020).
- ²D. Bacorisen, R. Smith, J. A. Ball, R. W. Grimes, B. P. Uberuaga, K. E. Sickafus, and W. T. Rankin, “Molecular dynamics modelling of radiation damage in normal, partly inverse and inverse spinels,” *Nucl. Instrum. Methods Phys. Res., Sect. B* **250**, 36–45 (2006).
- ³B. P. Uberuaga, D. Bacorisen, R. Smith, J. A. Ball, R. W. Grimes, A. F. Voter, and K. E. Sickafus, “Defect kinetics in spinels: Long-time simulations of Mg Al₂O₄, MgGa₂O₄, and Mg In₂O₄,” *Phys. Rev. B* **75**, 104116 (2007).
- ⁴T. Ohira, Y. Inoue, K. Murata, and J. Murayama, “Magnetite scale cluster adhesion on metal oxides surfaces: Atomistic simulation study,” *Appl. Surf. Sci.* **171**, 175–188 (2001).
- ⁵G. Y. Lai, *High-Temperature Corrosion and Materials Applications* (ASM International, 2007).

- ⁶M. Hoppe, *Magnetic, Structural, and Electronic Properties of NiFe₂O₄ Ultrathin Films* (Forschungszentrum Jülich, Jülich, 2016), ISBN: 978-3-95806-122-4.
- ⁷H. J. Reichmann and S. D. Jacobsen, "High-pressure elasticity of a natural magnetite crystal," *Am. Mineral.* **89**, 1061–1066 (2004).
- ⁸H. Salazar-Tamayo, K. E. G. Tellez, and C. A. B. Meneses, "Cation vacancies in NiFe₂O₄ during heat treatments at high temperatures: Structural, morphological and magnetic characterization," *Mater. Res.* **22**, e20190298 (2019).
- ⁹S. B. Narang and K. Pubby, "Nickel spinel ferrites: A review," *J. Magn. Magn. Mater.* **519**, 167163 (2021).
- ¹⁰Ö. N. Avci, L. Sementa, and A. Fortunelli, "Mechanisms of the oxygen evolution reaction on NiFe₂O₄ and CoFe₂O₄ inverse-spinel oxides," *ACS Catal.* **12**, 9058–9073 (2022).
- ¹¹F. Cheng, J. Shen, B. Peng, Y. Pan, Z. Tao, and J. Chen, "Rapid room-temperature synthesis of nanocrystalline spinels as oxygen reduction and evolution electrocatalysts," *Nat. Chem.* **3**, 79–84 (2011).
- ¹²C. L. Muhich, V. J. Aston, R. M. Trotter, A. W. Weimer, and C. B. Musgrave, "First-principles analysis of cation diffusion in mixed metal ferrite spinels," *Chem. Mater.* **28**, 214–226 (2016).
- ¹³F. Liu, J. Dai, J. Liu, Y. Yang, and R. Fang, "Density functional theory study on the reaction mechanism of spinel CoFe₂O₄ with CO during chemical-looping combustion," *J. Phys. Chem. C* **123**, 17335–17342 (2019).
- ¹⁴Zs. Rák, C. J. O'Brien, and D. W. Brenner, "First-principles investigation of boron defects in nickel ferrite spinel," *J. Nucl. Mater.* **452**, 446–452 (2014).
- ¹⁵N. W. Grimes, "Self-diffusion in compounds with spinel structure," *Philos. Mag.* **25**, 67–76 (1972).
- ¹⁶R. Sun, "Diffusion of cobalt and chromium in chromite spinel," *J. Chem. Phys.* **28**, 290–293 (1958).
- ¹⁷H. Salazar-Tamayo, K. E. García, and C. A. Barrero, "New method to calculate Mössbauer recoilless f-factors in NiFe₂O₄. Magnetic, morphological and structural properties," *J. Magn. Magn. Mater.* **471**, 242–249 (2019).
- ¹⁸Z. Ž Lazarević, Č. Jovalekić, A. Milutinović, D. Sekulić, V. N. Ivanovski, A. Rečnik, B. Cekić, and N. Ž Romčević, "Nanodimensional spinel NiFe₂O₄ and ZnFe₂O₄ ferrites prepared by soft mechanochemical synthesis," *J. Appl. Phys.* **113**, 187221 (2013).
- ¹⁹L. I. Granone, A. C. Ulpe, L. Robben, S. Klimke, M. Jahns, F. Renz, T. M. Gasing, T. Bredow, R. Dillert, and D. W. Bahnemann, "Effect of the degree of inversion on optical properties of spinel ZnFe₂O₄," *Phys. Chem. Chem. Phys.* **20**, 28267–28278 (2018).
- ²⁰R. C. Kambale, N. R. Adhate, B. K. Chougule, and Y. D. Kolekar, "Magnetic and dielectric properties of mixed spinel Ni–Zn ferrites synthesized by citrate–nitrate combustion method," *J. Alloys Compd.* **491**, 372–377 (2010).
- ²¹A. Navrotsky and O. J. Kleppa, "Thermodynamics of formation of simple spinels," *J. Inorg. Nucl. Chem.* **30**, 479–498 (1968).
- ²²K. E. Sickafus, J. M. Wills, and N. W. Grimes, "Structure of spinel," *J. Am. Ceram. Soc.* **82**, 3279–3292 (2004).
- ²³K. Tapasa, A. V. Barashev, D. J. Bacon, and Yu. N. Osetsky, "Computer simulation of carbon diffusion and vacancy–carbon interaction in α -iron," *Acta Mater.* **55**, 1–11 (2007).
- ²⁴A. F. Voter, "Introduction to the kinetic Monte Carlo method," in *Radiation Effects in Solids*, edited by K. E. Sickafus, E. A. Kotomin, and B. P. Uberuaga (Springer Netherlands, Dordrecht, 2007), pp. 1–23.
- ²⁵D. Perez, B. P. Uberuaga, Y. Shim, J. G. Amar, and A. F. Voter, "Chapter 4 accelerated molecular dynamics methods: Introduction and recent developments," in *Annual Reports in Computational Chemistry*, edited by R. A. Wheeler (Elsevier, 2009), pp. 79–98.
- ²⁶G. Henkelman, B. P. Uberuaga, and H. Jónsson, "A climbing image nudged elastic band method for finding saddle points and minimum energy paths," *J. Chem. Phys.* **113**, 9901–9904 (2000).
- ²⁷B. P. Uberuaga and G. Pilania, "Inversion, chemical complexity, and interstitial transport in spinels," *J. Am. Ceram. Soc.* **104**, 2313–2324 (2021).
- ²⁸S. Hyun, H. Chun, M. Hong, J. Kang, and B. Han, "First-principles study on ultrafast Li-ion diffusion in halospinel Li₂Sc_{2/3}Cl₄ through multi-channels designed by aliovalent doping," *J. Mater. Chem. A* **11**, 4272–4279 (2023).
- ²⁹N. Mousseau, L. K. Béland, P. Brommer, F. El-Mellouhi, J.-F. Joly, G. K. N[†]Tsouaglo, O. Restrepo, and M. Trochet, "Following atomistic kinetics on experimental timescales with the kinetic activation–relaxation technique," *Comput. Mater. Sci.* **100**, 111–123 (2015).
- ³⁰F. El-Mellouhi, N. Mousseau, and L. J. Lewis, "Kinetic activation-relaxation technique: An off-lattice self-learning kinetic Monte Carlo algorithm," *Phys. Rev. B* **78**, 153202 (2008).
- ³¹L. K. Béland, P. Brommer, F. El-Mellouhi, J.-F. Joly, and N. Mousseau, "Kinetic activation-relaxation technique," *Phys. Rev. E* **84**, 046704 (2011).
- ³²P. Brommer and N. Mousseau, "Comment on 'mechanism of void nucleation and growth in bcc Fe: Atomistic simulations at experimental time scales,'" *Phys. Rev. Lett.* **108**, 219601 (2012).
- ³³B. D. McKay, "Practical graph isomorphism," in *Proceedings of the 10th Manitoba Conference on Numerical Mathematics and Computing, Winnipeg, 1–4 October 1980, Congressus Numerantium (Utilitas Mathematica, 1981)*, Vol. 30, pp. 45–87.
- ³⁴B. D. McKay and A. Piperno, "Practical graph isomorphism, II," *J. Symb. Comput.* **60**, 94–112 (2014).
- ³⁵G. T. Barkema and N. Mousseau, "Event-based relaxation of continuous disordered systems," *Phys. Rev. Lett.* **77**, 4358–4361 (1996).
- ³⁶R. Malek and N. Mousseau, "Dynamics of Lennard-Jones clusters: A characterization of the activation-relaxation technique," *Phys. Rev. E* **62**, 7723–7728 (2000).
- ³⁷E. Machado-Charry, L. K. Béland, D. Caliste, L. Genovese, T. Deutsch, N. Mousseau, and P. Pochet, "Optimized energy landscape exploration using the ab initio based activation-relaxation technique," *J. Chem. Phys.* **135**, 034102 (2011).
- ³⁸B. Puchala, M. L. Falk, and K. Garikipati, "An energy basin finding algorithm for kinetic Monte Carlo acceleration," *J. Chem. Phys.* **132**, 134104 (2010).
- ³⁹Ö. A. Restrepo, Ö. Arnache, J. Restrepo, C. S. Becquart, and N. Mousseau, "Comparison of bulk basic properties with different existing Ni-Fe-O empirical potentials for Fe₃O₄ and NiFe₂O₄ spinel ferrites," *Comput. Mater. Sci.* **213**, 111653 (2022).
- ⁴⁰A. Pedone, G. Malavasi, M. C. Menziani, A. N. Cormack, and U. Segre, "A new self-consistent empirical interatomic potential model for oxides, silicates, and silica-based glasses," *J. Phys. Chem. B* **110**, 11780 (2006).
- ⁴¹L. Deng and J. Du, "Development of boron oxide potentials for computer simulations of multicomponent oxide glasses," *J. Am. Ceram. Soc.* **102**, 2482–2505 (2019).
- ⁴²W. Sun and J. Du, "Interfacial structures of spinel crystals with borosilicate nuclear waste glasses from molecular dynamics simulations," *J. Am. Ceram. Soc.* **102**, 4583–4601 (2019).
- ⁴³P. M. Oliver, G. W. Watson, and S. C. Parker, "Molecular-dynamics simulations of nickel oxide surfaces," *Phys. Rev. B* **52**, 5323–5329 (1995).
- ⁴⁴J. Vaari, "Molecular dynamics simulations of vacancy diffusion in chromium(III) oxide, hematite, magnetite and chromite," *Solid State Ionics* **270**, 10–17 (2015).
- ⁴⁵S. Plimpton, "Fast parallel algorithms for short-range molecular dynamics," *J. Comput. Phys.* **117**, 1–19 (1995).
- ⁴⁶See <http://lammps.sandia.gov/index.html> for Lammmps web site.
- ⁴⁷H. Perron, T. Mellier, C. Domain, J. Roques, E. Simoni, R. Drot, and H. Catalette, "Structural investigation and electronic properties of the nickel ferrite NiFe₂O₄: A periodic density functional theory approach," *J. Phys.: Condens. Matter* **19**, 346219 (2007).
- ⁴⁸X. Shi, "First principles studies of the surface chemistry of NiFe₂O₄ and Ni_xCo_{3-x}O₄ spinel oxides," Ph.D. dissertation (Princeton University, 2018), pp. 102–106, <http://arks.princeton.edu/ark:/88435/dsp01b5644v312>.
- ⁴⁹H. Shiiba, N. Zetsu, M. Nakayama, S. Oishi, and K. Teshima, "Defect Formation energy in spinel LiNi_{0.5}Mn_{1.5}O_{4-δ} using ab initio DFT calculations," *J. Phys. Chem. C* **119**, 9117–9124 (2015).
- ⁵⁰J. J. Melo Quintero, K. L. Salcedo Rodríguez, C. E. Rodríguez Torres, and L. A. Errico, "Ab initio study of the role of defects on the magnetic response and the structural, electronic and hyperfine properties of ZnFe₂O₄," *J. Alloys Compd.* **775**, 1117–1128 (2019).
- ⁵¹L. Pauling, "The principles determining the structure of complex IONIC crystals," *J. Am. Chem. Soc.* **51**, 1010–1026 (1929).

⁵²L. Yin, B. J. Kwon, Y. Choi, C. J. Bartel, M. Yang, C. Liao, B. Key, G. Ceder, and S. H. Lapidus, “Operando X-ray diffraction studies of the Mg-ion migration mechanisms in spinel cathodes for rechargeable Mg-ion batteries,” *J. Am. Chem. Soc.* **143**, 10649–10658 (2021).

⁵³Ó. A. Restrepo, Ó. Arnache, J. Restrepo, C. S. Becquart, and N. Mousseau, “Structural modeling of ZnFe_2O_4 systems using Buckingham potentials with static molecular dynamics,” *Solid State Commun.* **354**, 114914 (2022).